machines

Article

Analysis of the Control Characteristics of the Electro-Hydraulic Vibration System Based on the Single-Neuron Control Algorithm

Wenang Jia [1,2,*], Zeji Chen [1], Tongzhong Chen [1] and Sheng Li [1,2]

[1] College of Mechanical Engineering, Zhejiang University of Technology, Hangzhou 310023, China; 2112102054@zjut.edu.cn (Z.C.); 2111902209@zjut.edu.cn (T.C.); lishengjx@zjut.edu.cn (S.L.)
[2] Key Laboratory of Special Purpose Equipment and Advanced Processing Technology, Ministry of Education and Zhejiang Province, Zhejiang University of Technology, Hangzhou 310023, China
* Correspondence: jiawenang@zjut.edu.cn

Abstract: This paper proposes an electro-hydraulic vibration control system based on the single-neuron PID algorithm, which improves the operating frequency of the electro-hydraulic fatigue testing machine and the control accuracy of the load force. Through mathematical modeling of the electro-hydraulic vibration system (EVS), a MATLAB/Simulink simulation, and experimental testing, this study systematically analyzes the output waveform of the EVS as well as the closed-loop situation of load force amplitude and offset under the action of the single-neuron PID algorithm. The results show that: the EVS with a 2D vibration valve as the core, which can control the movement of the spool in the two-degrees-of-freedom direction, can realize the output of an approximate sinusoidal load force waveform from 0 to 800 Hz. The system controlled by the single-neuron PID algorithm is less complex to operate than the traditional PID algorithm. It also has a short rise time for the output load force amplitude curve and a maximum control error of only 1.2%. Furthermore, it exhibits a rapid closed-loop response to the load force offset. The range variability of the load force is measured to be 1.43%. A new scheme for the design of EVS is provided in this study, which broadens the application range of electro-hydraulic fatigue testing machines.

Keywords: electro-hydraulic vibration system; 2D vibration valve; single-neuron PID algorithm; load force closed-loop control

Citation: Jia, W.; Chen, Z.; Chen, T.; Li, S. Analysis of the Control Characteristics of the Electro-Hydraulic Vibration System Based on the Single-Neuron Control Algorithm. *Machines* **2024**, *12*, 58. https://doi.org/10.3390/machines12010058

Academic Editor: Zheng Chen

Received: 23 November 2023
Revised: 22 December 2023
Accepted: 10 January 2024
Published: 12 January 2024

1. Introduction

With the rapid advancements in machinery, aerospace, and technology, the demand for new materials is on the rise [1]. This has led to the optimization of various mechanical structures and processes through iterative processes, which, in turn, has increased the requirements for the longer fatigue life of mechanical components [2]. Over the last century, experts in fields such as ultra-high perimeter fatigue, creep fatigue, in situ fatigue, and finite element analysis have conducted extensive research on metal fatigue [3]. They have concluded that fatigue damage in metal materials starts with the development of fatigue cracks, and these cracks' expansion is uncertain. Therefore, numerous scholars have established models and formulas to understand the fatigue cracks' expansion process in metal fatigue [4–8]. Fatigue tests that require large load forces can take several days or even weeks to complete due to the limited operating frequency of the testing machine. This lengthy testing cycle not only hinders the progress of new material research and development but also increases the number of unstable factors. Therefore, the development of a high-frequency vibration system for fatigue testing machines is of great theoretical and practical significance.

A fatigue testing machine is a piece of equipment used to test the performance and durability of materials. It involves various fields such as mechanics, hydraulics, electronics, and materials [9]. An electro-hydraulic fatigue testing machine is a type of fatigue testing machine that combines electrical and hydraulic test equipment. It mainly consists of a hydraulic cylinder, a tank, a hydraulic pump, and electro-hydraulic servo valves. With its enormous load-to-weight ratio and convenient amplitude and frequency parameter adjustments, this fatigue testing apparatus is highly effective. It is also possible to control the alternating load force waveform's output. The most popular kind of testing apparatus for fatigue testing is this kind of machine. Sebastian et al. have designed a large-scale constructed resonance bending fatigue tester to shorten the fatigue life testing time of train track specimens and reduce energy costs. Compared with the traditional fatigue testing machine, this machine increases the vibration frequency from 5 Hz to 20 Hz, which significantly shortens the fatigue test time and, at the same time, can be used for the bending fatigue testing of large specimens with a span of up to 13 m and a loading frequency of 50 Hz, and it reduces the energy consumption of the machine by utilizing the principle of resonance [10]. Erena et al. designed a fatigue test device capable of testing different types, configurations, and lengths of cables and strands. The device is capable of applying axial loads and bending moments simultaneously to produce damage to the specimen [11]. Torres Duart et al. designed a biaxial fatigue machine operating at 1.2 Hz to perform tensile-torsional fatigue testing on Nafion 115 material in controlled environments of humidity and temperature [12]. Ogawa et al. developed a multiaxial non-proportional load fatigue testing machine, which utilizes the inertial forces generated by the rotation of the rotating wheels on both sides to perform combined torsion and bending experiments and realizes a high-cycle multiaxial fatigue test with an operating frequency of 50 Hz [13]. Yürük et al. designed and built a computer-based fatigue testing machine to perform 10 Hz fatigue tests on dissimilar aluminum alloys (AA5754/AA6013) welded using friction stir welding. It provides insights for future research on the welding results of dissimilar aluminum alloys and dynamic loading of welded joints [14]. ISAKOV et al. designed a 48 Hz large-scale fatigue tester based on the rotating beam method to reduce the errors arising from the use of data from small specimens to infer the fatigue performance of large components, which can test high-strength specimens with a gauge diameter of 32 mm and a gauge length of 100 mm [15]. Ko et al. designed a 5 Hz electrohydraulic fatigue machine capable of simultaneously fatiguing eight clamps of a rail fastening system, which shortens the time required for fatigue testing and reduces the cost of the experiment [16]. The existing general-purpose electro-hydraulic fatigue testing machine is limited by the servo valve bandwidth, and its vibration frequency range is 2~200 Hz, such as the Landmark electro-hydraulic servo testing system of MTS [17], the 8872 hydraulic fatigue testing system of INSTRON [18], etc. To shorten the test time, scholars tend to carry out simultaneous tests for multiple targets or use the principle of resonance to enhance the test frequency of the test specimen.

Control algorithms have become increasingly important in fatigue testing machine control systems due to the rapid development of computer technology. Liao et al. aimed at the wind blade fatigue test process coupling effect for the synchronization of the two exciters, designed a PID algorithm as the core of the virtual master synchronization control algorithm, conducted a numerical simulation of the synchronization control algorithm of the stable convergence of the analysis, and verified the effectiveness of the synchronization control algorithm [19]. Adam Heyduk et al. implemented the MCS controller in a fatigue testing machine and achieved improved control results [20]. Ma et al. designed a fatigue testing system that uses fuzzy PID control, powered by an AC servo electric cylinder. The displacement is measured using an extensometer and used as feedback for the control system. This system improves the dynamic response speed by 16% compared to traditional PID-controlled fatigue testing machines [21]. Moncy et al. proposed two biaxial cyclic strain control algorithms as fatigue testing strategies for composite materials. The two control algorithms were tested on an MTS biaxial testing machine. The results revealed that the maximum error in peak feedback strain was 6.4% and 9.0% for the active and passive control methods, respectively, and the active control method had a higher accuracy compared to the passive control method. However, the fidelity of the active control method decreases when the system loses track of the point markers [22]. Zhao et al. designed a cross-compensation control algorithm to solve the serious coupling phenomenon between multiple loading channels in the aircraft structural fatigue test system. The controller output signal can be cross-compensated by the algorithm to increase the operating speed of the test equipment by 15% [23]. Duan et al. proposed an optimized PID controller based on an improved non-dominated sorting genetic algorithm (NSGA-III) to significantly improve the dynamic tracking accuracy of the fatigue testing machine, in response to the problem that the actual vibration frequency and amplitude of aviation flexible connectors are lower than the set values during fatigue testing on the fatigue testing machine [24].

The current development of the electro-hydraulic fatigue testing machine has yielded remarkable results and expanded its field of application to a wider range of materials. However, the current electro-hydraulic fatigue testing machine uses an electro-hydraulic servo valve with the slide valve structure in the vibration system. Due to the effect of reciprocating inertial force, the vibration frequency of this fatigue testing machine is limited to a maximum of 200 Hz. Compared to the slide valve structure, the rotary valve is not affected by inertial forces and can significantly increase the operating frequency by increasing the rotational speed. This study aims to overcome the 200 Hz working-frequency limitation of the existing electro-hydraulic fatigue testing machine by utilizing the 2D vibration valve with the structure of the rotary valve as the core. This will enable the electro-hydraulic vibration system to work at a higher frequency of 800 Hz. In the field of fatigue testing machine control, PID control algorithms are widely used. The conventional PID algorithm requires a significant amount of time to readjust the parameters when the operating frequency of the fatigue testing machine changes to ensure the output load force curve. To improve control accuracy and adaptive performance, an EVS was designed using the self-learning and self-adaptive characteristics of a single-neuron PID algorithm. This paper examines the load force output of the vibration system under the action of a single-neuron PID algorithm, as well as the actual control effect of load force amplitude under different algorithms, through a theoretical analysis, a MATLAB/Simulink (R2018b) simulation, and experimental tests, to confirm the viability of the design scheme.

The remainder of this paper is organized as follows. Section 2 of the report introduces the electro-hydraulic fatigue testing machine and explains the working principle of the 2D electro-hydraulic exciter, which has a 2D vibration valve as its core component. Section 3 describes the mathematical modeling of the 2D electro-hydraulic exciter as well as the PID controller. Section 4 details the simulation of the EVS, followed by Section 5 which describes the construction of the test bench. The results of both the simulation and experimentation are analyzed in Section 6, with a summary provided in Section 7.

2. 2D Electro-Hydraulic Vibration System

2.1. Electro-Hydraulic Vibration System Structure

Figure 1 illustrates the composition of an electro-hydraulic fatigue testing machine. The core of the vibration system comprises a 2D electro-hydraulic exciter and a controller. The 2D electro-hydraulic exciter consists of several components such as a force transducer, specimen, hydraulic cylinder, displacement transducer, 2D vibration valves, and bias servo valves. On the other hand, the controller comprises the main control panel and the upper computer. The system's main control panel regulates the position of the hydraulic cylinder's piston rod using the bias servo valve and the 2D vibration valve. This results in the generation of feedback signals from the displacement sensor and the force sensor. These signals are then transmitted to the main control panel of the system, decoded, and analyzed by the main control chip. This enables the system to obtain data such as the amplitude of the vibration force, offset value, and other related information.

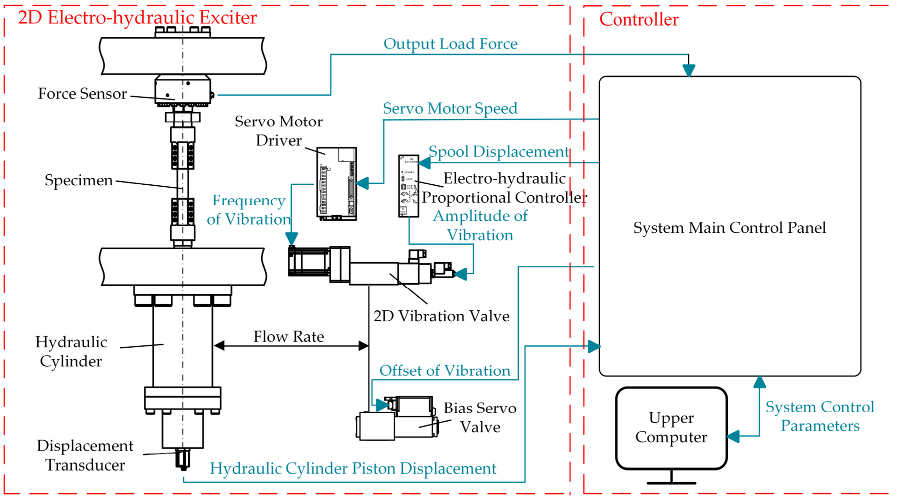

Figure 1. Structural diagram of the electro-hydraulic vibration system.

2.2. 2D Vibration Valve Structure and Working Principle

The structure of the 2D vibration valve is shown in Figure 2. The periodic flow of oil into the two chambers of the hydraulic cylinder is achieved through the spool shoulder groove and the valve sleeve rectangular window, which alternately opens and closes. This motion causes the hydraulic cylinder piston rod to move back and forth. The 2D vibration valve consists of several components, including servo motor, gearbox, sleeve, spring, spool, valve sleeve, valve body, plug assembly, and proportion electro-magnet. The 2D vibration valve combines the features of slide valve axial movement and rotary valve circumferential rotation. The spool circumferential rotation manages the frequency of oil switching, while the spool axial displacement controls the oil flow. A servo motor controls the rotary movement of the spool, while a proportional electro-magnet controls the axial displacement of the spool. The servo motor is connected to the large gear at the left end of the gearbox, and the sleeve is connected to the small gear at the right end. The gearbox amplifies the servo motor speed, driving the sleeve and spool to rotate at high speeds.

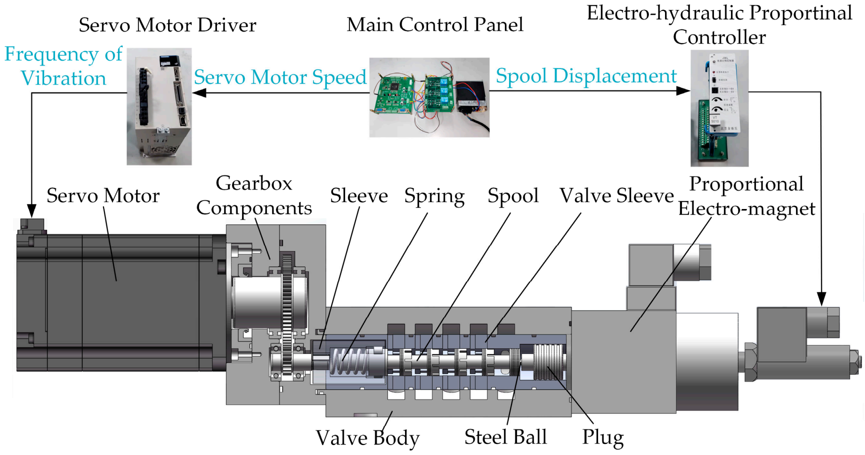

Figure 2. 3D structural diagram of the 2D vibration valve.

As shown in Figure 3a, mounted on the valve body's right end face is the proportional electro-magnet. In a non-functioning 2D vibration valve, the sleeve's spring pushes the spool back to its starting position through a return force; in a functioning 2D vibration valve, the plug assembly transfers the proportionate electro-magnet armature displacement to the spool, compressing the sleeve's spring and allowing the spool to remain in a specific rotational position. This allows for the control of the 2D vibration valve's oil-switching frequency and flow rate. The plug transmits the axial force to the spool through the steel ball, and the steel ball and the right end face of the spool transmit the axial force in a point-contact manner, which can reduce friction in the process of the high-speed rotation of the spool. As shown in Figure 3b, the flow rate through the spool is proportional to the axial displacement and has a sinusoidal-like relationship with the circumferential angle. When the spool rotates at high speeds, as shown in Figure 3c, the amplitude of pressure change at the working port is inversely proportional to the spool's rotation speed.

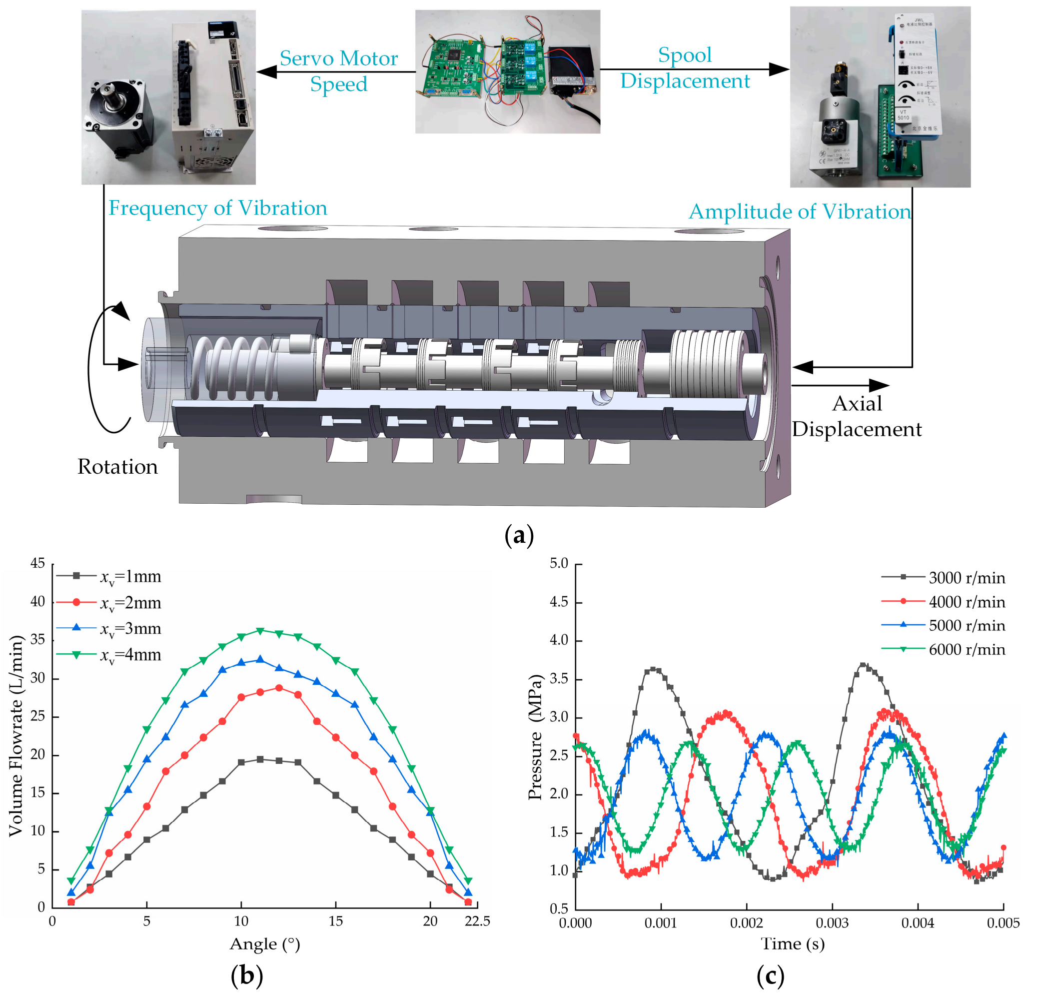

Figure 3. The characteristics of 2D vibration valves. (**a**) The 2D vibration-valve working diagram; (**b**) static characteristics; (**c**) dynamic characteristics.

The operation of the 2D vibration valve is shown in Figures 4 and 5. The valve sleeve of the 2D vibration valve has eight circumferential rectangular windows that are evenly arranged, and the valve spool has four working steps arranged in a sequence. Each step has eight grooves that are uniformly arranged in the circumferential direction, with a 22.5° phase difference in the opening angle of the grooves of neighboring steps in the circumferential direction. When the spool of the vibration valve is rotated from 0° to 22.5°, as shown in Figure 4, high-pressure oil passes through the P port. The oil then flows from the throttle port at step III through the grooves into the valve cavity formed by steps III and IV. It then enters into the cavity at the right end of the exciter cylinder through the B port to drive the piston rod of the exciter cylinder to translate to the left. The oil flows from the left end chamber of the hydraulic cylinder through port A into the valve chamber composed of steps I and II, and finally returns to the oil tank through the throttle port at step I.

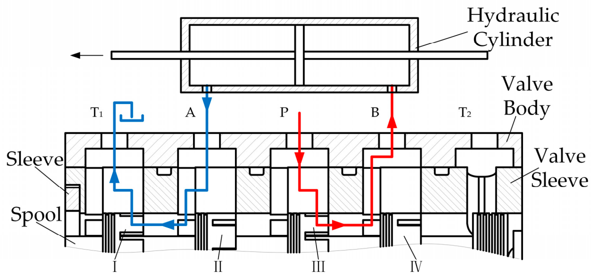

Figure 4. The spool rotates at 11.25°.

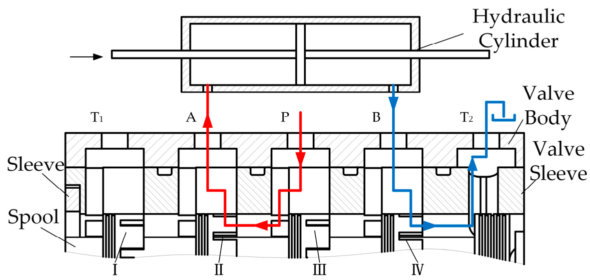

Figure 5. The spool rotates at 33.75°.

Figure 5 shows that when the spool is rotated from 22.5° to 45°, high-pressure oil passes through the P port and enters the valve cavity, which is made up of steps II and III, from the throttling port at step III. The oil then enters the left end chamber of the exciter cylinder through the A port, driving the piston rod to move to the right. Subsequently, the oil flows from the right end chamber of the hydraulic cylinder through port B into the valve chamber, consisting of step IV and the guiding step, before finally returning to the oil tank through port T_2.

So far, the piston rod of the hydraulic cylinder in the high-pressure oil promotes the realization of a back-and-forth reciprocating motion. The spool rotation of a circle can push the hydraulic cylinder to realize eight times the reciprocating motion. With the help of the gearbox, the servo motor can make the spool reach a speed of 6000 r·min^{-1}, which is four times faster than its original speed. This enables the vibration system to work at a frequency of over 800 Hz.

3. Mathematical Modeling

The EVS is simplified to the schematic diagram shown in Figure 6. The spool of the 2D vibration valve moves both in circular and linear directions, where $A_{s1} \sim A_{s4}$, $A_{v1} \sim A_{v4}$ are the valve port area of the bias servo valve and the 2D vibration valve, respectively; $T_1 \sim T_2$ are the drain port of the 2D vibration valve; P_s is the pressure of the oil source; P_1 and P_2 are the oil ports pressure at the left and right ends of the hydraulic cylinder, respectively; y_p is the displacement of the hydraulic cylinder piston.

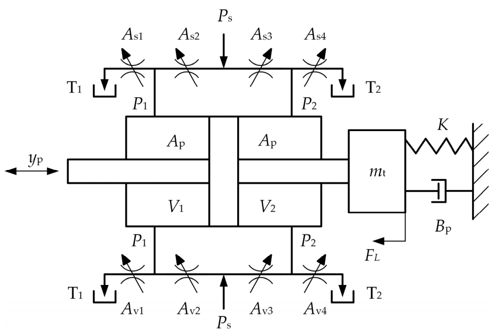

Figure 6. Schematic diagram of the composition of the 2D electro-hydraulic exciter.

3.1. 2D Electro-Hydraulic Exciter

The throttle port area of the 2D vibration valve is created by the overlap between the spool shoulder groove and the rectangular window of the valve sleeve. As shown in Figure 7, the throttle port has a rectangular shape, with its long side x_v generated by the axial displacement of the spool. The width y_{di} of the throttle port changes periodically with the circumferential rotation of the spool. The opening angle of the valve spool and valve sleeve is represented by θ, and the overlap angle is formed by the overlap side length y_{di} for a section of the arc. Since both the overlap side length and the arc radius are relatively small, the section of the arc can be simplified as a straight line. Therefore, the shape of the throttle port of the vibration valve can be equated to a planar rectangle. Furthermore, the gradient of the throttle port area is determined by the axial displacement of the spool x_v, and the rate of change of the throttle port area is related to the circumferential rotation speed of the spool.

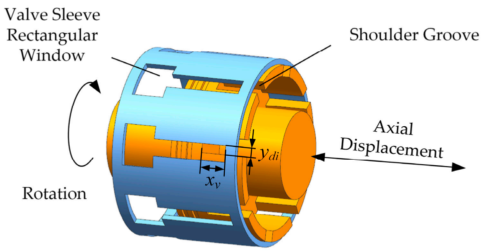

Figure 7. Schematic diagram of the valve port area of the 2D vibration valve.

The 2D vibration valve overlap area is calculated as:

$$A_{d1} = \begin{cases} 2Zx_vR\sin\frac{\alpha}{2} & \alpha \in [4j\theta, (4j+1)\theta) \\ 2Zx_vR\sin(\theta - \frac{\alpha}{2}) & \alpha \in [(4j+1)\theta, (4j+2)\theta) \\ 0 & \alpha \in [(4j+2)\theta, (4j+3)\theta) \\ 0 & \alpha \in [(4j+3)\theta, (4j+4)\theta] \end{cases} \tag{1}$$

$$A_{d2} = \begin{cases} 0 & \alpha \in [4j\theta, (4j+1)\theta) \\ 0 & \alpha \in [(4j+1)\theta, (4j+2)\theta) \\ 2Zx_vR\sin(\frac{\alpha}{2} - \theta) & \alpha \in [(4j+2)\theta, (4j+3)\theta) \\ 2Zx_vR\sin(2\theta - \frac{\alpha}{2}) & \alpha \in [(4j+3)\theta, (4j+4)\theta] \end{cases} \tag{2}$$

where A_{d1} is the overlap area of spool step I(III) and sleeve opening; A_{d2} is the overlap area of spool step II(IV) and sleeve opening; Z is the number of circumferential grooves of a single spool step of the 2D vibration valve; R is the outer contour of the spool step and the inner wall radius of the sleeve; α is the angle of rotation of the spool; θ is the angle of the spool step and the sleeve groove; $j \in N$ is the number of vibration cycles.

Comparing Equations (1) and (2) to Figure 6, The relationship between the area $A_{v1} \sim A_{v4}$ of the 2D vibration valve's throttle port and A_{d1} can be obtained.

$$\begin{cases} A_{d1} = A_{v1} = A_{v3} \\ A_{d2} = A_{v2} = A_{v4} \end{cases} \tag{3}$$

The vibration system's motor's rotation speed n and the rotation angle α of the spool of the vibration valve are related as follows:

$$\alpha = 2\pi \cdot \frac{z_1}{z_2} \cdot \frac{n}{60} \cdot t \tag{4}$$

where z_1 is the number of teeth of the large gear of the gearbox; z_2 is the number of teeth of the pinion gear of the gearbox; n is the rotation speed of the servo motor; t is the rotation time of the motor.

Assuming the 2D vibration valve has a symmetrical structure, the flow rate of the throttle port at each shoulder can be determined using the throttling equation:

$$\begin{cases} Q_{jz1} = C_d A_{v1} \sqrt{\frac{2}{\rho} P_1} \\ Q_{jz2} = C_d A_{v2} \sqrt{\frac{2}{\rho} (P_s - P_1)} \\ Q_{jz3} = C_d A_{v3} \sqrt{\frac{2}{\rho} (P_s - P_2)} \\ Q_{jz4} = C_d A_{v4} \sqrt{\frac{2}{\rho} P_2} \end{cases} \tag{5}$$

where Q_{jzi} is the flow rate at A_{vi}, $i = 1, 2, 3, 4$; C_d is the flow coefficient of the 2D vibration valve orifice; ρ is the density of oil..

The relationship between the input signal of the bias servo valve and the area of the valve port is:

$$A_{pz} = \frac{\frac{Q_{pz}}{60000}}{C_d \sqrt{\frac{2}{\rho} \cdot \Delta p}} \cdot \frac{1}{|u_{pz\max}|} \cdot u_{opz} \tag{6}$$

where A_{pz} is the orifice area of the bias servo valve; Q_{pz} is the rated flow rate of the bias servo valve; Δp is the pressure difference between the front and rear of the bias servo valve ports; $u_{pz\max}$ is the maximum signal of the bias servo valve input control; u_{opz} is the input control signal of the bias servo valve.

The 2D vibration valve and bias servo valves are connected in parallel in the two cavities of the hydraulic cylinder, and the joint equation is obtained:

$$\begin{cases} Q_1 = Q_{jz2} - Q_{jz1} + Q_{pz2} - Q_{pz1} \\ Q_2 = Q_{jz3} - Q_{jz4} + Q_{pz3} - Q_{pz4} \end{cases} \tag{7}$$

where Q_1 is the flow rate of the left cavity of the hydraulic cylinder; Q_2 is the flow rate of the right cavity of the hydraulic cylinder; Q_{pzi} is the bias servo valve port flow, $i = 1, 2, 3, 4$.

The flow continuity equation for the hydraulic cylinder is:

$$\begin{cases} Q_1 = A_p \frac{dy_p}{dt} + C_{ip}(P_1 - P_2) + C_{ep} P_1 + \frac{V_1}{\beta_e} \frac{dP_1}{dt} \\ Q_2 = A_p \frac{dy_p}{dt} + C_{ip}(P_1 - P_2) - C_{ep} P_1 - \frac{V_2}{\beta_e} \frac{dP_2}{dt} \end{cases} \tag{8}$$

where A_p is the effective area of the hydraulic cylinder piston; y_p is the displacement of the hydraulic cylinder piston; C_{ip} is the internal leakage coefficient of the hydraulic cylinder; C_{ep} is the external leakage coefficient of the hydraulic cylinder; V_1 is the volume of the left end of the hydraulic cylinder chamber; V_2 is the volume of the right end of the hydraulic cylinder chamber; β_e is the equivalent volume elastic modulus.

The 2D vibration valve spool's circumferential rotation can be compared to the axial movement of the spool in a two-position three-way slide valve. This means that the load flow rate of the vibration system can be calculated using the flow balance principle of the bridge circuit.

$$q_L = \frac{Q_{jz2} - Q_{jz1} + Q_{pz2} - Q_{pz1}}{2} + \frac{Q_{jz4} - Q_{jz3} + Q_{pz4} - Q_{pz3}}{2} \tag{9}$$

where q_L is the load flow rate of the hydraulic cylinder in the system.

The force balance equation of the hydraulic cylinder piston is:

$$p_L A_p = m_t \frac{d^2 y_p}{dt^2} + B_p \frac{dy_p}{dt} + K y_p + F_L \tag{10}$$

where p_L is the load pressure of the hydraulic cylinder; m_t is the total mass of the piston rod of the hydraulic cylinder and the load; B_p is the viscous damping coefficient of the vibration system; K is the elastic load stiffness of the vibration system; F_L is the external load force on the piston of the hydraulic cylinder.

The linearization theory is used to analyze the dynamics of the valve-controlled-cylinder system. The Laplace transform of the analyzed results is obtained:

$$Q_L = K_q Y_d - K_c P_L \tag{11}$$

where K_q is the zero-opening flow gain of the 2D vibration valve; Y_d is the length of the overlap between the spool and the total throttling port of the valve sleeve; K_c is the flow-pressure coefficient of the 2D vibration valve.

The relational equation of the total throttle port overlap side length produced by the rotation of the spool of the 2D vibration valve of the vibration system and the output displacement of the hydraulic cylinder piston under the condition of having an elastic load can be obtained by combining the aforementioned Equations (7)–(10) Laplace-transformed and (11):

$$Y_p = \frac{\frac{K_q}{A_p}Y_d - \frac{K_{ce}}{A_p^2}\left(1 + \frac{V_t}{4\beta_e K_{ce}}s\right)F_L}{\frac{V_t m_t}{4\beta_e A_p^2}s^3 + \left(\frac{K_{ce} m_t}{A_p^2} + \frac{V_t B_p}{4\beta_e A_p^2}\right)s^2 + \left(1 + \frac{V_t K}{4\beta_e A_p^2}\right)s + \frac{K_{ce}K}{A_p^2}}$$

The above equation is converted into a transfer function of the 2D vibration cylinder piston output force F to the command input Y_d:

$$\frac{F}{Y_d} = \frac{\frac{KK_q}{A_p}}{\frac{V_t m_t}{4\beta_e A_p^2}s^3 + \left(\frac{K_{ce} m_t}{A_p^2} + \frac{V_t B_p}{4\beta_e A_p^2}\right)s^2 + \left(1 + \frac{V_t K}{4\beta_e A_p^2}\right)s + \frac{K_{ce}K}{A_p^2}}$$

The above equation is organized to give:

$$\frac{F}{Y_d} = \frac{\left(\frac{K_{ps}A_p}{K}\right)\cdot K}{\left(\frac{s}{\omega_r} + 1\right)\left(\frac{s^2}{\omega_0^2} + \frac{2\zeta_0}{\omega_0}s + 1\right)} \tag{12}$$

where $\frac{K_{ps}A_p}{K}$ is the position gain of the elastically loaded vibration system; ω_r and ω_0 are the turning frequency of the inertial and second-order oscillatory links of the system; ζ_0 is the integrated damping ratio.

3.2. Controller

The calculation formula for the output signal of the force transducer is:

$$u_{sen} = \frac{u_{ref}c_{nom}}{f_{nom}}\cdot F \tag{13}$$

where u_{ref} is the supply voltage; c_{nom} is the calibration value; f_{nom} is the rated force of the force transducer; u_{sen} is the output signal of the force transducer; F is the output load force of the hydraulic cylinder collected by the force transducer.

For the proportional electro-magnet with the bias servo valve, the input and output are calculated as follows:

$$\begin{cases} u_{obi} = k_{bi}u_{ibi} \\ u_{opz} = k_{pz}u_{ipz} + b \end{cases} \tag{14}$$

where u_{obi} is the proportional electro-magnet control input signal; k_{bi} is the proportional electro-magnet amplifier circuit gain; u_{ibi} is the amplitude control analog signal output from the main control chip; u_{opz} is the bias servo valve control input signal; k_{pz} is the bias servo valve amplifier circuit gain; u_{ipz} is the offset control analog signal output from the main control chip; b is the bias servo valve op amp circuit offset error value.

The horizontal displacement of the proportional electro-magnet actuator is calculated as:

$$x_v = k_v u_{obi} \tag{15}$$

where x_v is the horizontal displacement of the proportional electro-magnet actuator (spool axial displacement); k_v is the proportional electro-magnet conversion factor.

$$n = 60 \cdot \frac{f}{Z} \cdot \frac{z_2}{z_1} \tag{16}$$

where f is the EVS vibration frequency.

3.3. The Single-Neuron PID Algorithm

To strengthen the regulation accuracy and anti-disturbance capability of the EVS, a single-neuron PID control algorithm is selected to optimize the control system.

The unsupervised Hebb learning mechanism expression is:

$$\Delta w_{ij}(k) = \eta o_j(k) o_i(k) \tag{17}$$

where $\Delta w_{ij}(k)$ is the connection weight between two neurons; η is the learning rate; $o_i(k)$ is the neuron activation value; $o_j(k)$ is the neuron activation value.

The expression for replacing $o_j(k)$ with a supervised Delta learning mechanism in Equation (17) is:

$$\Delta w_{ij}(k) = \eta(d_j(k) - o_j(k)) o_i(k) \tag{18}$$

where $d_j(k)$ is the ideal output; $o_j(k)$ is the actual output.

The supervised Hebb learning mechanism can be obtained by organizing Equations (17) and (18) with the expression [25–27]:

$$\begin{cases} u(k) = u(k-1) + K_m \sum\limits_{i=1}^{3} w'_i(k) x_i(k) \\ w'_i(k) = w_i(k) / \sum\limits_{i=1}^{3} |w_i(k)| \\ w_1(k) = w_1(k-1) + \eta_I e(k) u(k) x_1(k) \\ w_2(k) = w_2(k-1) + \eta_P e(k) u(k) x_2(k) \\ w_3(k) = w_3(k-1) + \eta_D e(k) u(k) x_3(k) \end{cases} \tag{19}$$

$$\begin{cases} x_1(k) = e(k); \\ x_2(k) = e(k) - e(k-1); \\ x_3(k) = e(k) - 2e(k-1) + e(k-2); \end{cases}$$

where $u(k)$ is the output value of the kth time; $u(k-1)$ is the output value of the $k-1$th time; K_m is the neuron scale factor; $w'_i(k)$ is the weight value of the dendrites i under the learning rule; $w_i(k)$ is the activation value of the dendrites i of the kth time; $w_i(k-1)$ is the activation value of the dendrites $k-1$ of the ith time; $x_i(k)$ is the dendrites of a single-neuron, $i = 1, 2, 3$; η_I is the integral learning rate; η_P is the proportional learning rate; η_D is the differential learning rate; $e(k)$ is the bias value of the kth time; $e(k-1)$ is the bias value of the $k-1$th time; $e(k-2)$ is the bias value of the $k-2$th time.

4. The Simulation Analysis

A simulation model of a double-outlet-rod hydraulic cylinder controlled by the 2D vibration valve was constructed using the proposed 2D electro-hydraulic exciter mathematical model on the MATLAB/Simulink platform. The constructed model was used to analyze the stability of the vibration system. Additionally, controllers and modules such as

S-Function Builder were added to investigate the amplitude of the vibration force and the offset of the EVS, while considering the simulation model as a precondition.

4.1. 2D Electro-Hydraulic Exciter

As depicted in Figure 8, the flow simulation module of the 2D vibration valve was established according to Equation (5), and the flow rate of each valve port of the 2D vibration valve was calculated from the pressure of the valve port of the 2D vibration valve and the area of the throttle port; then, the simulation module of the continuity equation of the hydraulic cylinder was established through the associative Equations (7)–(9) to obtain the pressure of the left and right cavities of the hydraulic cylinder. Finally, the output load force of the hydraulic cylinder's piston was obtained through the hydraulic cylinder and load force balance equation module constructed using Equation (10). The output force of the vibration system was set as the output interface, while the spool groove and the length of the overlapping sides of the rectangular window were set as the input command interface. This allows for conducting the stability analysis of the EVS. The initial parameters for the EVS are listed in Table 1.

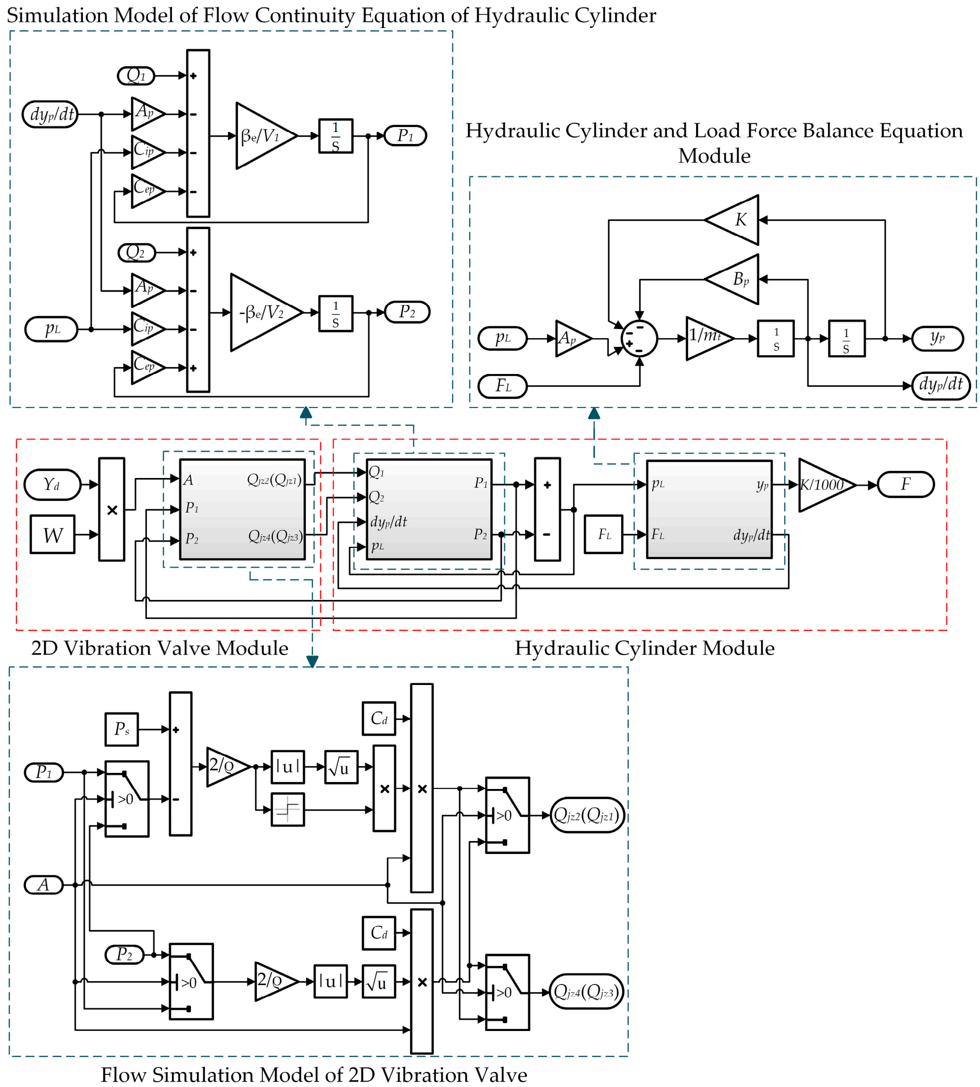

Figure 8. Simulation diagram of stability analysis of the vibration system.

Table 1. Main parameters of electro-hydraulic vibration system for fatigue test.

Parameters (Units)	Value
Z	8
C_d	0.62
W (m)	0.004
P_s (Pa)	3×10^6
ρ (kg/m^3)	870
A_p (m^2)	2.64×10^{-2}
V_t (m^3)	5.28×10^{-3}
m_t (kg)	40
β_e (Pa)	7×10^8
K (N/m)	1×10^9

Figure 9 makes it clear that the amplitude characteristic curve is above zero and that the EVS has an integrated intrinsic frequency of 919.7 Hz. The EVS's output load force curve declines with increasing vibration frequency in the [0, 919.7) Hz frequency range. When the vibration system gets close to the second-order oscillation link's turning frequency, it resonates. The degree of resonance deepens until it reaches its maximum at 919.7 Hz. The vibration system is obviously a second-order oscillation system based on the figure.

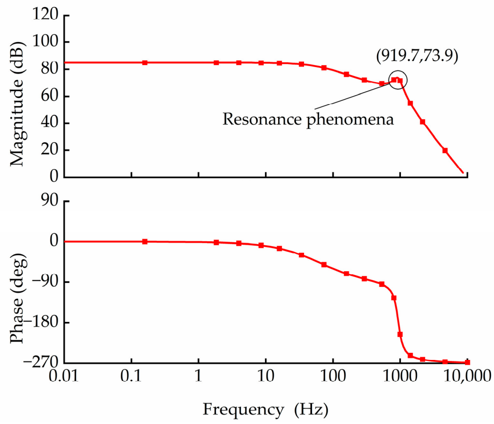

Figure 9. Bode diagram of the electro-hydraulic vibration system.

When the vibration frequency exceeds 919.7 Hz, the phase lag of the output load force of the vibration system deepens, and the amplitude of the output load force decreases continuously. To shorten the fatigue test time while maintaining the output of the system's load force, the vibration frequency can be adjusted to the second-order oscillation link adjacent to the turning frequency of the system so that the vibration system with elastic loads can maintain a stable output of the load force at high vibration frequencies.

The analog voltage signal output by the force sensor is relatively weak. Therefore, an op-amp circuit in the instrument must be used to amplify the signal, as illustrated in Figure 10. The vibration waveform peak-to-peak and offset acquisition module calculates the peak-to-peak and mean values of the output waveforms based on the force sensor output signals at different spool angles.

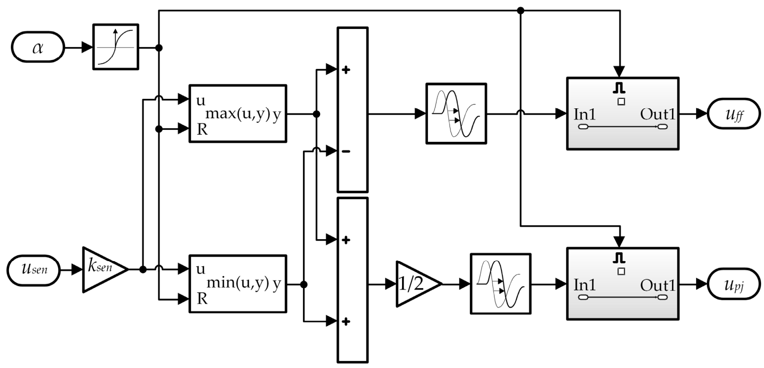

Figure 10. Vibration waveform peak-to-peak and offset acquisition module.

4.2. Electro-Hydraulic Vibration System

As shown in Figure 11, the stability analysis model of the vibration system was combined with the proportional solenoid valve, bias servo valve, and servo motor control circuit simulation module built with Equations (14)–(16), the vibration valve throttling port area simulation module built with Equations (1)–(4), the bias servo valve flow rate simulation module built with Equation (6) and the throttling equation, and the force sensor simulation module built with Equation (13), the vibration waveform peak-to-peak value and offset acquisition module together form the electro-hydraulic vibration system model. The amplitude and offset of the EVS model were simulated and analyzed on the MATLAB/Simulink platform. On this basis, the PID control program was written in the S-Function Builder module, and the closed-loop simulation of the amplitude and offset of the EVS was carried out. The closed-loop simulation of the electro-hydraulic vibration is shown in Figure 11. The control parameters are shown in Table 2. Where $FFPeak\_Valley\_Value$ is the amplitude feedback input; $PZAverage\_Valve$ is the offset feedback input; $FFoutput\_val$ is the amplitude output value; $PZoutput\_val$ is the offset output value.

In the closed-loop simulation of the EVS's vibration amplitude, the area A of the 2D vibration valve throttle port is changed by adjusting u_{ibi} to control the axial movement of the valve spool. This changes the output force F of the vibration cylinder, which is collected by the force sensor, and the peak-to-peak value u_{ff} of the vibration waveform is calculated from the output signals u_{sen} of the stress sensor according to the different spool angles α. The deviation from the target value is calculated by comparing u_{ff} with the single-neuron PID algorithm, and the resulting deviation value is used as an input parameter to change u_{ibi}. When the deviation value is zero, the EVS achieves the goal of the closed-loop vibration amplitude. This PID closed-loop controller maintains real-time control until the test is terminated in subsequent work. The basic principle of offset closed-loop is the same as that of amplitude closed-loop, and the offset closed-loop control of the EVS is finally realized by changing the value of u_{ipz}.

Table 2. The parameters of single-neuron PID controller in the simulation experiment.

Controller	Parameter Name	Notation	Value
Amplitude close loop	Neuron scale factor	*FFK*	0.0006
	Integral learning rate	*FFEta_i*	8
	Proportional learning rate	*FFEta_p*	0.2
	Differential learning rate	*FFEta_d*	0.1
	Step signal	*FFTARGET*	300
Offset close loop	Neuron scale factor	*PZK*	0.24
	Integral learning rate	*PZEta_i*	400
	Proportional learning rate	*PZEta_p*	500
	Differential learning rate	*PZEta_d*	0.1
	Step signal	*PZTARGER*	300

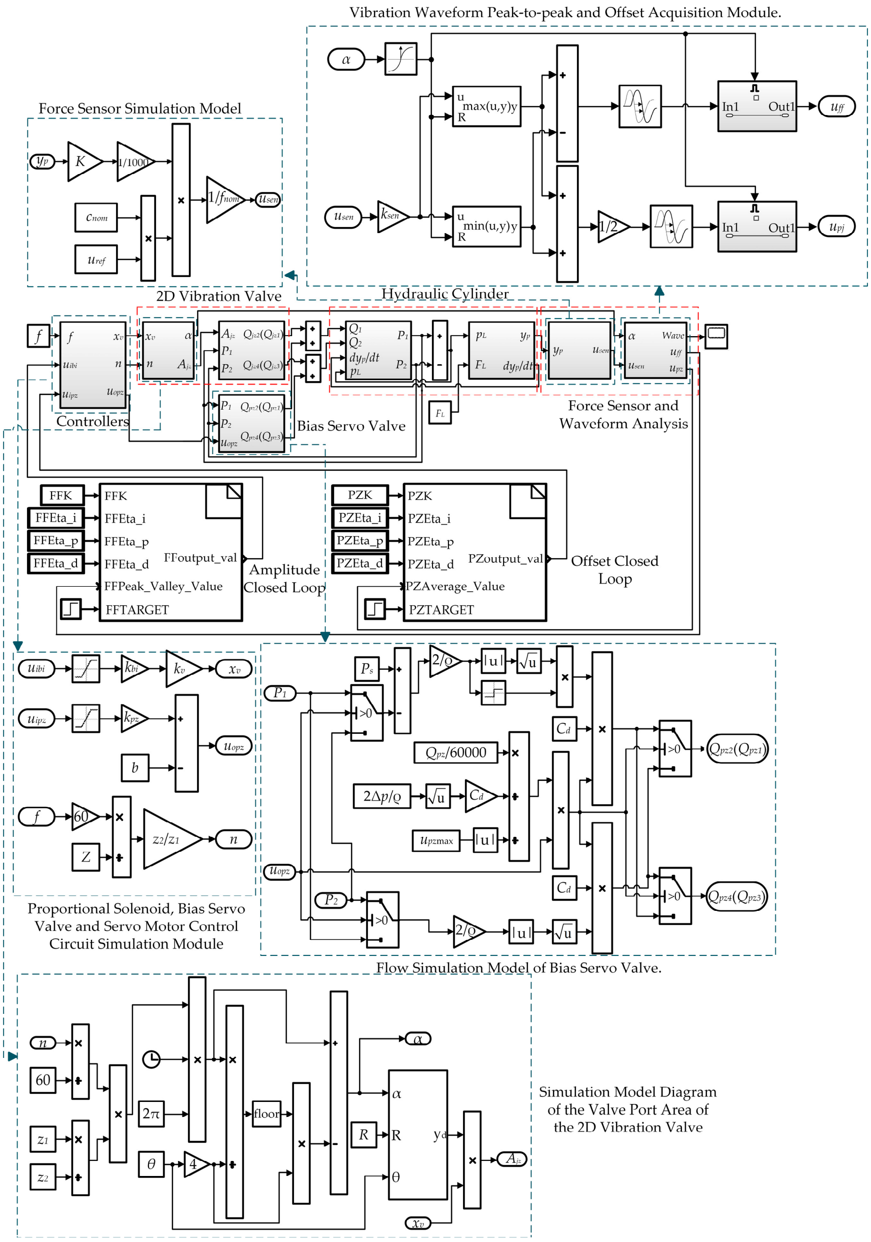

Figure 11. Electro-hydraulic vibration system amplitude and offset closed-loop simulation diagram.

5. Experimental Equipment and Programs

An electro-hydraulic fatigue testing machine was constructed as a test platform to study and verify the amplitude control of the vibration system under different algorithms, as well as the actual control effect of the single-neuron PID control algorithm on the EVS. Table 3 shows some of the components and sensor parameters used. In Figure 12, the force transducer and fixture are secured using bolts, and the fixture fixes the specimen and is connected to the piston rod of the hydraulic cylinder through the holes in the base of the fatigue test bench. The bottom of the hydraulic cylinder is connected to the displacement sensor, and the EVS is engaged. The load force is transferred to the force transducer through the fixture and the specimen, and the displacement data of the piston rod are obtained by the displacement sensor. In Figure 13, the bias servo valve and the vibration valve oil circuit are connected in parallel to the two chambers of the hydraulic cylinder. The gearbox ratio is 1:4, and the system control box is responsible for controlling the rotation of the servomotor and the proportional electromagnet horizontal displacement. The lower computer uses the STM32F429IGT6 main control chip as the controller core, which receives and analyzes the signals of each sensor of the system and sends command signals to each system module. The upper computer interface is written using the LabView platform to enable human–computer interaction.

Table 3. Components and transducer selection for the electro-hydraulic vibration systems.

Component	Type	Parameters
Force sensor	U10M-250kN, HBM, GER	Range: 0~250 kN, precision: 0.03
Displacement sensor	RHM0100MD601V010100, MTS, USA	Range: 0~100 mm, resolution: 1.5 μm
Servo motor	SGM7A, YASKAWA, JPN	Rated speed: 0~3000 r·min^{-1}, rated output: 1 kw
Proportional electro-magnet	GP61-4-A, HNAY, CHN	Rated stroke: 0~4.5 mm, repeatable accuracy: ≤1%
Oscilloscope	MSO-X 3054A, KEYSIGHT, USA	Acquisition frequency: 500 MHz

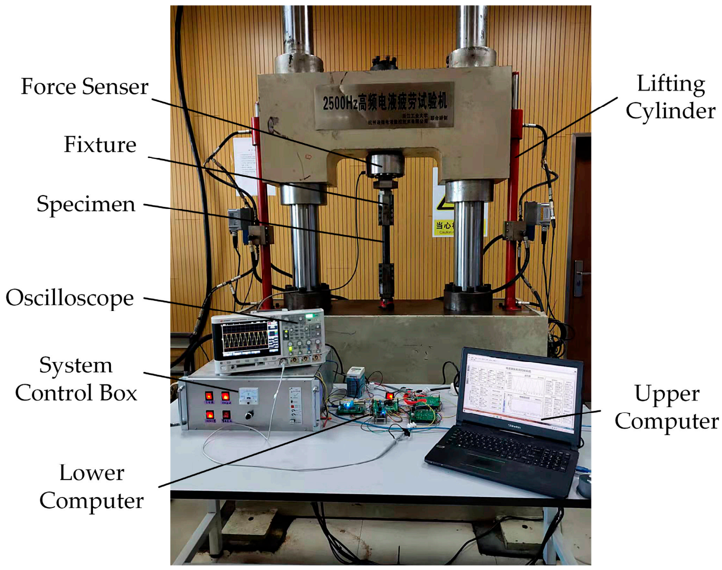

Figure 12. Electro-hydraulic fatigue test stages.

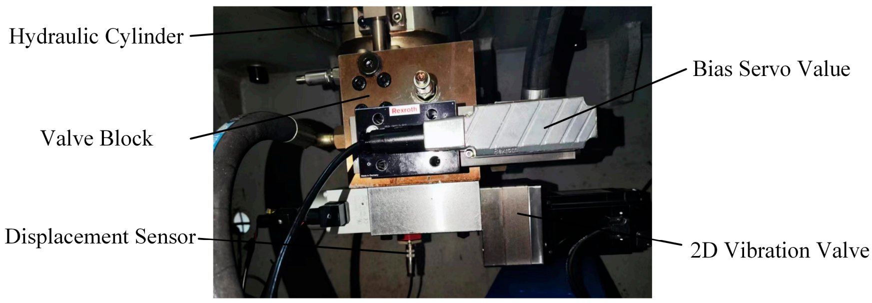

Figure 13. 2D Electro-hydraulic exciter.

6. The Analysis of Experimental and Simulation Results

6.1. The Open-Loop Experiment

The operating frequency of the EVS is controlled by the circumferential speed of the 2D vibration valve spool. The experiments were conducted with 3 MPa as the system oil supply pressure, and the axial displacements of the vibration valve spool were adjusted to be 1 mm, 2 mm, 3 mm, and 4 mm, respectively.

6.1.1. Amplitude of Load Force

The bias servo valve was set so that the EVS vibration waveform offset was zero. The vibration frequencies of 200 Hz, 400 Hz, 700 Hz, and 800 Hz waveforms were obtained as shown in Figure 14.

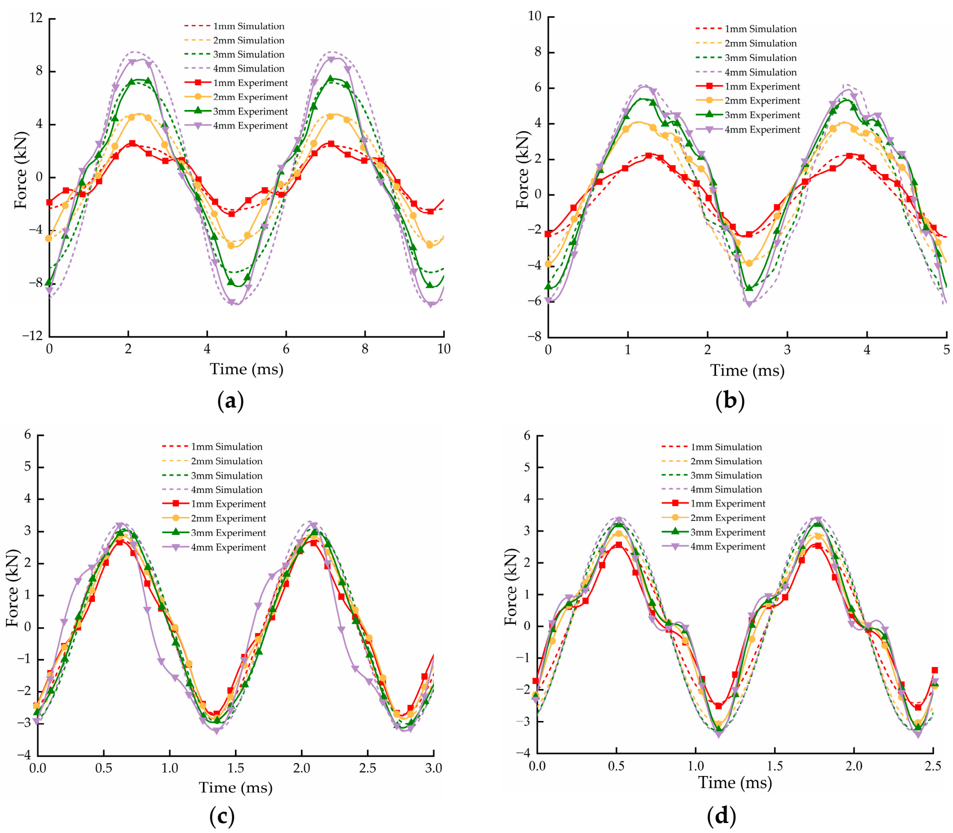

Figure 14. Waveform diagram of the vibration system. (**a**) 200 Hz; (**b**) 400 Hz; (**c**) 700 Hz; (**d**) 800 Hz.

When comparing the amplitude of the vibration waveform generated by different valve spool displacements at the same vibration frequency, it is evident that the output force of the EVS increases as the spool displacement of the vibration valve increases. The regulation of the amplitude of the vibration waveform is apparent with a low-frequency spool axial displacement on the EVS. However, as the vibration frequency of the system increases, the regulation by the spool axial displacement becomes weaker. This is mainly due to the fact that the hydraulic cylinder piston rod's output displacement of the EVS is small in the high-frequency band, leading to a small integrated damping ratio ζ_0. Consequently, the influence of the valve spool displacement on the hydraulic cylinder piston rod's output displacement becomes small as well. The amplitudes of the load force were 9.2 kN, 6.0 kN, 3.1 kN, and 3.4 kN at 200 Hz, 400 Hz, 700 Hz, and 800 Hz, respectively, when the spool displacement was 4 mm. The simulation results have the same trend with the experimental curves. From Figure 15, it can be seen that the amplitude–frequency characteristic curves are above the zero value; the vibration system is in the frequency interval [0, 800). With the increase in the vibration frequency, the vibration system's output load force firstly undergoes a significant decrease, and in the proximity of the system, the integrated intrinsic frequency rises to a certain degree, and the system undergoes a resonance phenomenon. The fatigue testing machine operating near the resonant frequency can effectively shorten the fatigue test time and accelerate the test sample's fatigue failure.

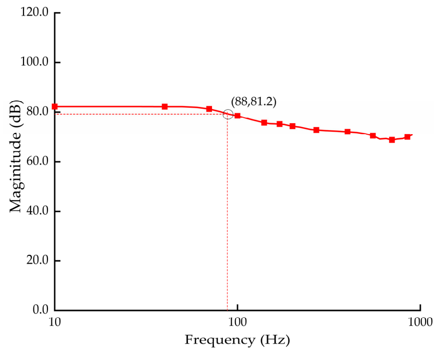

Figure 15. The amplitude–frequency characteristic curve of the vibration system.

After the output load force was stabilized, the amplitude fluctuation error of the output load force waveform at different frequencies was measured; the results are shown in Figure 16. The output load force of EVS fluctuates when it reaches the steady state, and the curve fluctuation is most obvious when the operating frequency is 600 Hz.

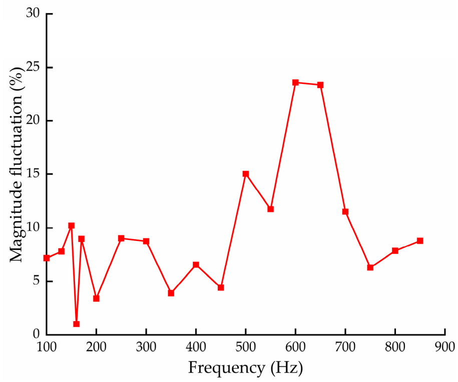

Figure 16. Load force amplitude fluctuations.

6.1.2. Offset of Load Force

During the experiment, the spool displacement of the 2D vibration valve was set to 2 mm, and the spool displacement of the bias servo valve was controlled to be positively and negatively biased in order to study the offset control characteristics of the system. The vibration waveforms of the EVS were adjusted for each vibration frequency by the offset, and the results are shown in Figure 17. The experiment conducted at frequencies between 200 Hz and 800 Hz shows that the EVS achieves the positive and negative bias of the vibration waveform under the control of the bias servo valve. This allows for the cyclic stress application of three types of specimens (tensile, compression, and tension-compression) to be realized in the testing machine. The experimental and simulation results were consistent with each other.

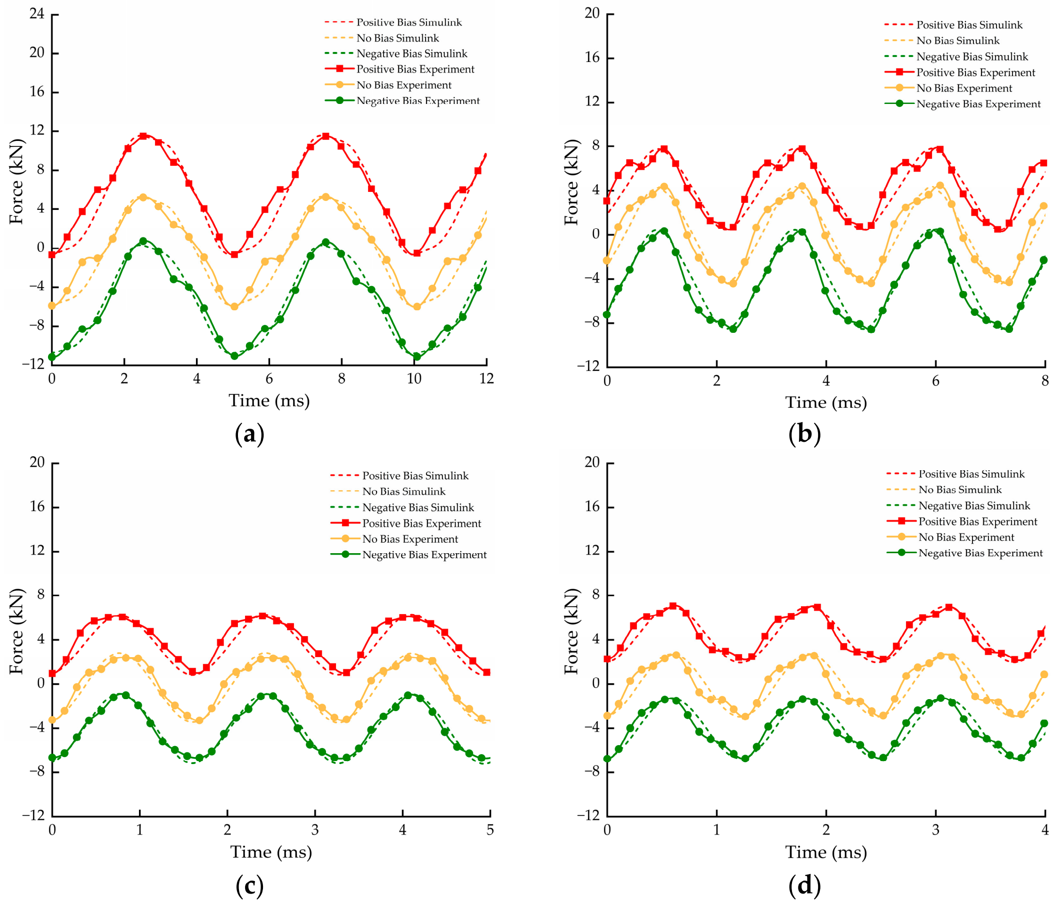

Figure 17. Offset waveform of the vibration system. (**a**) 200 Hz; (**b**) 400 Hz; (**c**) 600 Hz; (**d**) 800 Hz.

The load force output waveform is not strictly sinusoidal; it is an approximate sinusoidal waveform. To understand the degree of distortion of the vibration waveform, the distortion degree is used here for analysis. The distortion degree calculation formula is:

$$r = \frac{\sqrt{A_1^2 + A_2^2 + A_3^2 + A_4^2 + A_5^2 + \cdots}}{A_0} \times 100\% \tag{20}$$

where A_0 is the amplitude of the fundamental waveform of the vibration waveform; A_1, A_2, A_3, A_4, A_5,$\cdots$ are the amplitudes of the second, third, fourth, and fifth harmonics of the fundamental waveform, respectively.

The FFT transform of the vibration waveform from 200 Hz to 800 Hz is used to obtain load force spectrum as shown in Figure 18, and the distortion of the load force signal is calculated according to the harmonic components of each waveform as shown in Table 4.

The maximum distortion of the vibration waveform from 200 Hz to 800 Hz is 32.4%, and the vibration waveform of the vibration system has a certain degree of distortion at each frequency, which is not a standard sine wave. From the simulation waveform of the vibration system, it can be seen that the vibration waveform of the vibration system under ideal conditions has some distortion compared with the sinusoidal waveform. In addition, the narrow gap in the connecting parts of the experimental specimen fixture and the influence of the high-frequency resonance affect the load force conduction, which results in the large distortion of the output waveform.

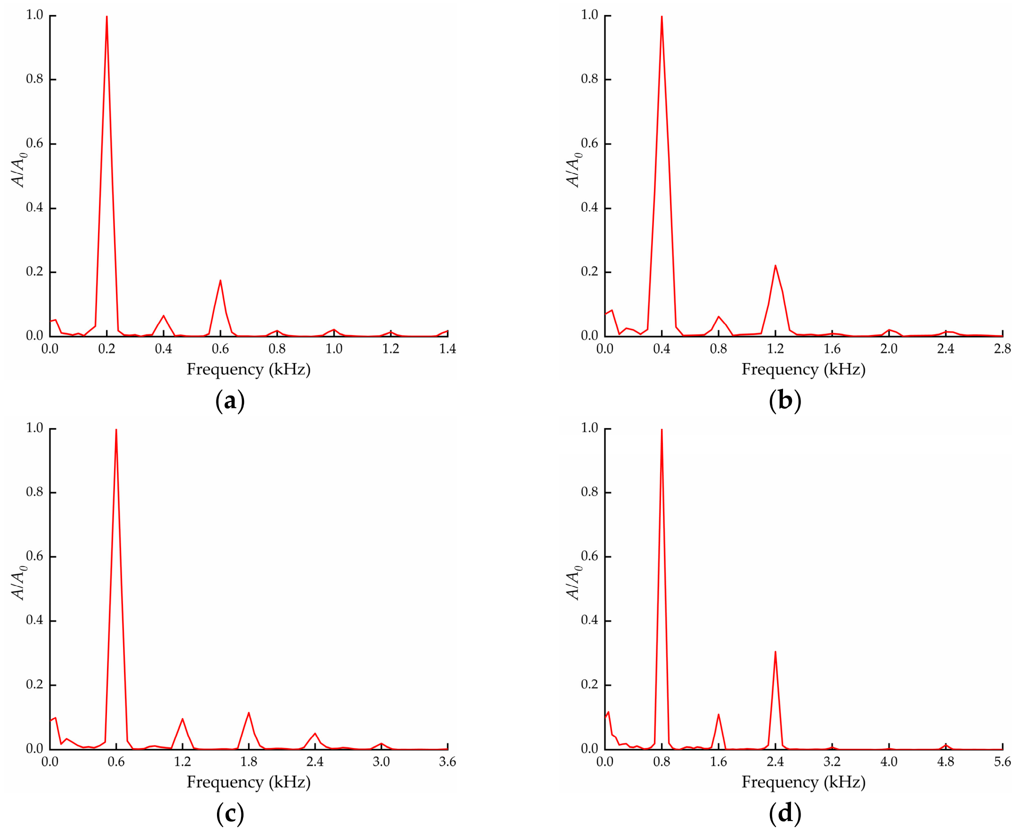

Figure 18. 200~800 Hz loading force spectrum. (**a**) 200 Hz; (**b**) 400 Hz; (**c**) 600 Hz; (**d**) 800 Hz.

Table 4. Root mean square value of load force and distortion at 200~800 Hz.

Frequency (Hz)	A_0/A_0	A_1/A_0	A_2/A_0	A_3/A_0	A_4/A_0	A_5/A_0	R (%)
200	1	0.0655	0.1759	0.0179	0.0211	0.0132	19.02
400	1	0.0627	0.2220	0.0088	0.0204	0.0142	23.22
600	1	0.0948	0.1148	0.0505	0.0185	0.0018	15.83
800	1	0.1093	0.3046	0.0071	0.003	0.0138	32.40

6.2. The Closed-Loop Experiment

The amplitude of the output load force decreases with increasing electro-hydraulic system vibration frequency. The output load force amplitude is maintained at a constant value by the PID algorithm's adjustment of the valve port's area. Furthermore, 3 MPa was the adjusted oil supply pressure. The conventional incremental PID needs to manually adjust the parameters again when the working conditions change, firstly, by adjusting the *Ki* value to control the output curve with a tendency to reach the steady state, and then by adjusting the *Kp* value to reduce the amplitude of the curve oscillation. When adjusting the *Kp* value cannot change the curve oscillation amplitude, it is necessary to reduce the *Ki* value and adjust the *Kp* value again, and finally adjust the *Kd* value to weaken the curve overshooting, which is a cumbersome and lengthy operational process. The single-neuron PID controls the curve by adjusting the *Km* value to obtain a faster rise time as well as a tendency to reach a steady state. The curve's sinusoidal decay and overshoot phenomenon are reduced by adjusting the η_P and η_I values, respectively; finally, the ideal curve is obtained by fine-tuning the η_D value. The single-neuron PID has the characteristic of self-learning and self-adaptation, so it can automatically adjust its parameters to maintain the load force stable output during the process of changing working conditions. The control parameters of the conventional PID are shown in Table 5 as the optimal parameters based on multiple debugging. Table 6 provides the single-neuron PID controller parameters.

Table 5. The parameters of conventional PID controller.

Frequency (Hz)	*Kp*	*Ki*	*Kd*
200	0.0002	0.0005	0
400	0.0001	0.0006	0
600	0.0001	0.001	0
800	0.0002	0.0008	0

Table 6. The parameters of single-neuron PID controller.

Parameters	Value
FFK	0.0004
FFEta_i	8
FFEta_p	0.2
FFEta_d	0.1
PZK	0.1
PZEta_i	400
PZEta_p	1000
PZEta_d	0.1

6.2.1. Different Algorithms for Load Force Amplitude Control

Targeting a load force of 2375.4 N (150 mV), the amplitude step curve of the EVS was observed using the traditional PID algorithm and the single-neuron PID algorithm, respectively, in order to reach the steady state at different frequencies. From Figure 19, it can be observed that the single-neuron PID algorithm, when tested at frequencies of 200 Hz, 400 Hz, 600 Hz, and 800 Hz, exhibits more adaptability as compared to the conventional PID algorithm. This results in a shorter time required for the system to reach a steady state. On the other hand, as shown in Figure 20, during the linear-frequency sweep experiment from 0 to 800 Hz, the conventional PID algorithm requires a longer adjustment time, and amplitude control error fluctuation was evident. Under the single-neuron PID control algorithm, the EVS displays self-learning and self-adaptive characteristics with a maximum load force amplitude control error of 1.2% and strong anti-interference.

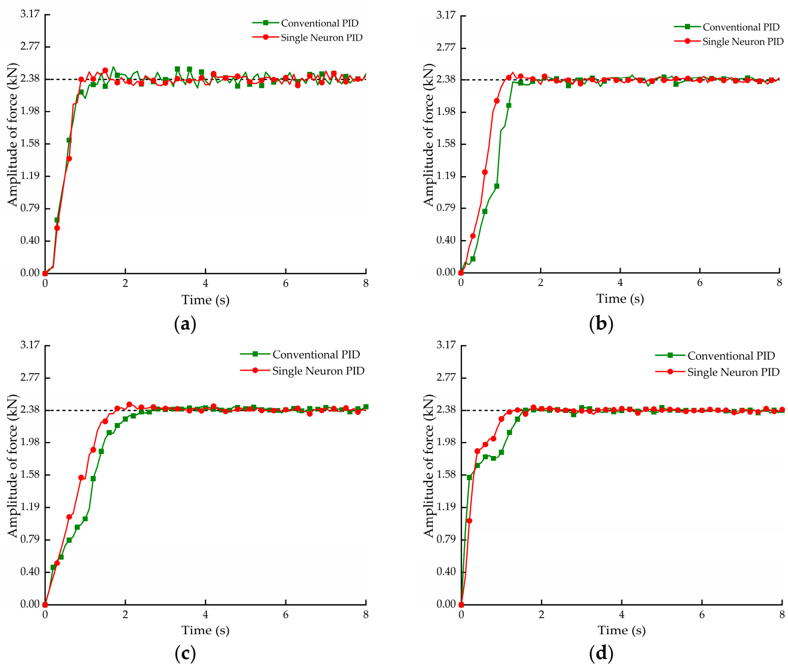

Figure 19. Comparison of closed-loop amplitude between the single-neuron PID and the conventional PID in the vibration system. (**a**) 200 Hz; (**b**) 400 Hz; (**c**) 600 Hz; (**d**) 800 Hz.

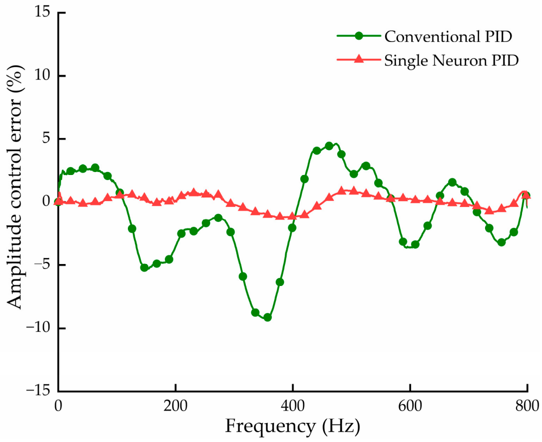

Figure 20. Amplitude control error curves under different algorithms.

6.2.2. Amplitude Control of Load Force

The position of the specimen was maintained by controlling the bias servo valve. Using a single-neuron PID algorithm, step response curves were generated for various frequencies with the target value set as the load force of 2375.4 N (150 mV). As depicted in Figure 21, the time taken for the amplitude step curve of the EVS to reach the steady state is 0.9 s (200 Hz), 1 s (400 Hz), 1.5 s (600 Hz), and 1 s (800 Hz), respectively. It is observed that the time required for the system to attain the steady state increases as the frequency rises from 200 Hz to 600 Hz. At 800 Hz, the EVS exhibits resonance, and the time taken for the system to reach the steady state decreases significantly. The amplitude step curves obtained from the simulation reach a steady state at different times for different frequencies, namely, 0.7 s (200 Hz), 1.5 s (400 Hz), 2.3 s (600 Hz), and 1.9 s (800 Hz). While the experimental results followed the same trend as the simulation, there is a slight deviation between the experimental results and the simulated curves. This deviation can be attributed to the hydrodynamic forces at the same frequency, and it becomes more significant with an increase in frequency. The 800 Hz EVS is affected by resonance, which causes a greater amplitude of the load force when the spool is opened. This results in a shorter time needed to reach the target value. The system combines a high vibration frequency with the resonance phenomenon to achieve a rapid closed-loop response, considering the characteristics of a high vibration frequency and large amplitude of the load force.

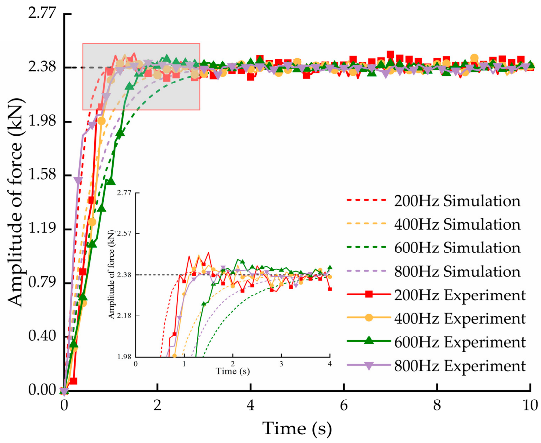

Figure 21. Amplitude step curve of the vibration system.

6.2.3. Offset Control of Load Force

The input voltage to the proportional electro-magnet was adjusted to displace the axial position of the spool in the 2D vibration valve by 2 mm. The EVS set the offset force to ±4750.8 N (±300 mV) as the target value and recorded the offset step curve of the EVS under the influence of the single-neuron PID algorithm. Figure 22 indicates that there is no significant change in the rising time of the offset step curve, while the frequency rises from 200 Hz to 800 Hz. The offset curves of the experiment and simulation exhibit the same overall trend. The experimental results demonstrate that the EVS can produce three types of offset effects, namely, compression, tension, and tension-compression, by controlling the bias servo valve. Under these three types of offset effects, the EVS can achieve a stable output of the load force.

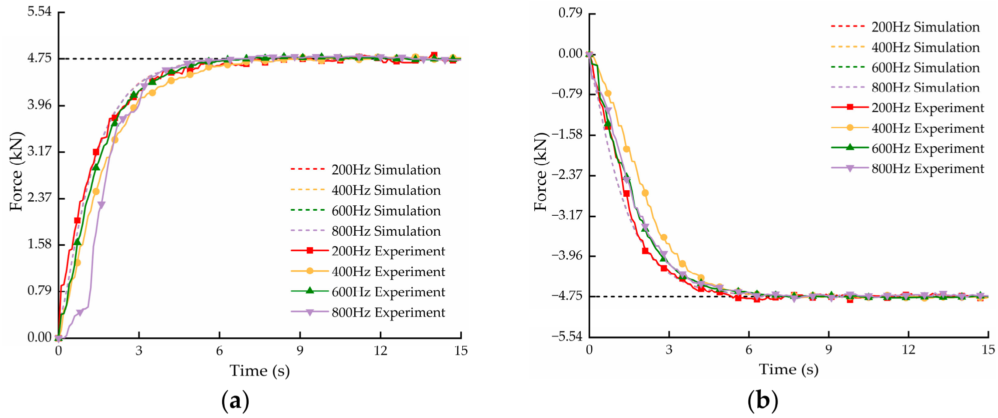

Figure 22. Offset step curve of the vibration system. (**a**) Positive bias; (**b**) negative bias.

The load force target amplitude range was set to 4750 N (±150 mV). The vibration offset force target values were set to −3167 N (−200 mV), 0 N (0 mV), and 3167 N (200 mV), respectively. The system activated the closed-loop control of the vibration amplitude and offset simultaneously, generating a vibration waveform as depicted in Figure 23. The waveform of the EVS is stable, indicating that the system could successfully implement the closed-loop control of the amplitude and offset at the same time. According to Table 7, the maximum variability of the load force range of the EVS is 1.43%. The EVS demonstrates a better closed-loop control of the load force amplitude and offset when subjected to the single-neuron PID algorithm.

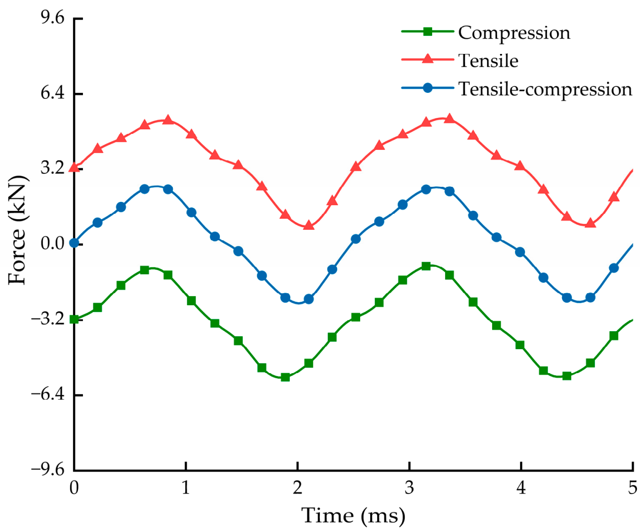

Figure 23. Vibration system amplitude and offset closed-loop waveform effects.

Table 7. Variation detection for different frequency force ranges.

Frequency (Hz)	Force Range Max (kN)	Force Range Min (kN)	Force Range Average (kN)	Range of Force Variability (%)
200	4.757	4.720	4.743	0.78
400	4.781	4.713	4.745	1.43
600	4.768	4.725	4.751	0.91
800	4.791	4.735	4.763	1.17

7. Conclusions

This paper explores the benefits of using a self-learning and self-adaptive single-neuron PID control algorithm in combination with the high operating frequency and high load of a 2D vibration valve to create an EVS. MATLAB/Simulink software and experimental testing were used to examine the stability of the system, the open-loop waveform output, and the closed-loop control effect which is under the single-neuron PID algorithm. The results of the experiments indicate that:

(1) The output waveform of the EVS approximated a sinusoidal waveform. With single-neuron PID control, the EVS could stably output a load force ranging from 0 to 800 Hz. This verified the feasibility of using the single-neuron PID control algorithm in EVSs by allowing for its control parameters to self-adjust according to the system parameters.

(2) The single-neuron PID algorithm provided superior independent closed-loop control of the load force amplitude and offset in the EVS. The EVS reached a steady state at different frequencies—0.9 s (200 Hz), 1 s (400 Hz), 1.5 s (600 Hz), and 1 s (800 Hz). When the frequency was 800 Hz, the EVS entered the resonant state, which provided the advantages of a large amplitude of the load force and a high operating frequency. The offset curve reached the steady state in a shorter response time. The EVS was able to stably output the load force even under the three offset effects of compression, tension, and tension-compression.

(3) The single-neuron PID algorithm significantly improved the closed-loop control of the load force amplitude and offset in the EVS, resulting in load force fluctuations of 0.78% (200 Hz), 1.43% (400 Hz), 0.91% (600 Hz), and 1.17% (800 Hz), respectively. The design of the EVS in this study further broadens the upper limit of the operating frequency of the EVS, reducing the limiting conditions of tested samples. This innovation can be used in the future for the high or ultra-high fatigue testing of aerospace materials such as TC4 titanium alloy and 7075 aluminum alloy.

Author Contributions: Conceptualization, W.J., Z.C. and S.L.; methodology, W.J., Z.C. and S.L.; software, W.J. and T.C.; validation, W.J., Z.C. and T.C.; formal analysis, W.J., Z.C. and S.L.; investigation, W.J., Z.C. and T.C.; resources, W.J., Z.C. and T.C.; data curation, W.J. and Z.C.; writing—original draft preparation, W.J., Z.C. and S.L.; writing—review and editing, W.J., Z.C. and S.L.; supervision, W.J., Z.C. and S.L.; project administration, W.J. and S.L.; funding acquisition, W.J. All authors have read and agreed to the published version of the manuscript.

Funding: This research was supported by Zhejiang Provincial Natural Science Foundation of China under Grant No.LY21E050015.

Data Availability Statement: The original contributions presented in the study are included in the article, further inquiries can be directed to the corresponding author.

Conflicts of Interest: The authors declare no conflicts of interest.

Nomenclature

Parameters	Meaning
x_v	Axial displacement of the spool
P_L	Hydraulic cylinder load pressure after Laplace transformation
K_{ce}	Total flow—pressure coefficient
V_t	Total compressed volume of hydraulic cylinder
W	Throttle area gradient
V_t	Total compressed volume of hydraulic cylinder
k_{sen}	Amplification factor for operational amplifier circuits
u_{ff}	Peak-to-peak value of the vibration waveform
u_{pz}	Vibration waveform offset value.
Kp	Proportional learning rate for the conventional PID
Ki	Integral learning rate for the conventional PID
Kd	Differential learning rate for the conventional PID
2D	Two-dimensiona
EVS	Electro-hydraulic vibration system

References

1. George, E.P.; Curtin, W.A.; Tasan, C.C. High Entropy Alloys: A Focused Review of Mechanical Properties and Deformation Mechanisms. *Acta Mater.* **2020**, *188*, 435–474. [CrossRef]
2. Linares, J.; Chaves-Jacob, J.; Lopez, Q.; Sprauel, J.-M. Fatigue Life Optimization for 17-4Ph Steel Produced by Selective Laser Melting. *Rapid Prototyp. J.* **2022**, *28*, 1182–1192. [CrossRef]
3. Xuan, F.; Zhu, M.; Wang, G. Retrospect and Prospect on Century-long Research of Structural Fatigue. *J. Mech. Eng.* **2021**, *57*, 26–51.
4. Romano, S.; Brückner-Foit, A.; Brandão, A.; Gumpinger, J.; Ghidini, T.; Beretta, S. Fatigue Properties of AlSi10Mg Obtained by Additive Manufacturing: Defect-Based Modelling and Prediction of Fatigue Strength. *Eng. Fract. Mech.* **2018**, *187*, 165–189. [CrossRef]
5. Liao, D.; Zhu, S.-P.; Keshtegar, B.; Qian, G.; Wang, Q. Probabilistic Framework for Fatigue Life Assessment of Notched Components under Size Effects. *Int. J. Mech. Sci.* **2020**, *181*, 105685. [CrossRef]
6. Carrara, P.; Ambati, M.; Alessi, R.; De Lorenzis, L. A Framework to Model the Fatigue Behavior of Brittle Materials Based on a Variational Phase-Field Approach. *Comput. Methods Appl. Mech. Eng.* **2020**, *361*, 112731. [CrossRef]
7. Li, X.-K.; Zhu, S.-P.; Liao, D.; Correia, J.A.F.O.; Berto, F.; Wang, Q. Probabilistic Fatigue Modelling of Metallic Materials under Notch and Size Effect Using the Weakest Link Theory. *Int. J. Fatigue* **2022**, *159*, 106788. [CrossRef]
8. Hectors, K.; De Waele, W. Cumulative Damage and Life Prediction Models for High-Cycle Fatigue of Metals: A Review. *Metals* **2021**, *11*, 204. [CrossRef]
9. Xu, Y. Trend of Hydraulic Technology in Industry 4.0 and its Intelligence Hydraulics. *Hydraul. Pneum. Seals* **2022**, *42*, 1–7.
10. Schneider, S.; Herrmann, R.; Marx, S. Development of a Resonant Fatigue Testing Facility for Large-Scale Beams in Bending. *Int. J. Fatigue* **2018**, *113*, 171–183. [CrossRef]
11. Erena, D.; Vázquez Valeo, J.; Navarro, C.; Domínguez, J. New Fatigue Device for Testing Cables: Design and Results. *Fatigue Fract. Eng. Mater. Struct.* **2019**, *42*, 1826–1837. [CrossRef]
12. Torres Duarte, L.M.; Domínguez Almaraz, G.M.; Torres Pacheco, C.J.; Zuñiga Tello, I.F. Device to Measure Fatigue Life of Membranes under Biaxial Loading Fatigue: Tension and Torsion. *Measurement* **2020**, *152*, 107382. [CrossRef]
13. Ogawa, F.; Shimizu, Y.; Bressan, S.; Morishita, T.; Itoh, T. Bending and Torsion Fatigue-Testing Machine Developed for Multiaxial Non-Proportional Loading. *Metals* **2019**, *9*, 1115. [CrossRef]
14. Yürük, A.; Çevik, B.; Kahraman, N. The Design of Fatigue Test Machine and the Analysis of Fatigue Behavior of FSWed Dissimilar Aluminum Alloys. *Exp. Tech.* **2023**, *47*, 591–601. [CrossRef]
15. Isakov, M.; Rantalainen, O.; Saarinen, T.; Lehtovaara, A. Large-Scale Fatigue Testing Based on the Rotating Beam Method. *Exp. Tech.* **2023**, *47*, 553–563. [CrossRef]
16. Ko, Y.-H.; Fang, X.-J.; Park, Y.-C.; Hu, J.-W.; Sim, H.-B. Development and Verification of Fatigue Testing Device for Rail Fastening Clamps. *Int. J. Steel Struct.* **2023**, *23*, 834–843. [CrossRef]
17. MTS. Landmark Electro-Hydraulic Servo Test System. Available online: https://www.mtschina.com/products/materials/dynamic-materials-test-systems/landmark-servohydraulic (accessed on 10 December 2023).
18. Table Top Fatigue Testing Systems | Instron. Available online: https://www.instron.com/en-us/products/testing-systems/dynamic-and-fatigue-systems/servohydraulic-fatigue/8872---8874 (accessed on 10 December 2023).
19. Liao, G.; Wu, J. Load Control of Vibration Exciter in Two-point Fatigue Test System of Wind Turbine Blade. *J. Tongji Univ. (Nat. Sci.)* **2018**, *46*, 11. [CrossRef]
20. Heyduk, A.; Kalinowski, K.; Kaula, R.; Pielot, J. Innovative Adaptive Control of Material Fatigue Test Machines Using an MCS Controller. *Multidiscip. Asp. Prod. Eng.* **2018**, *1*, 287–294. [CrossRef]

21. Ma, M.; Wang, H.; Deng, S.; Ni, Y.; Zhang, W. Research on fuzzy PID control system for fatigue testing machine based on LabVIEW. *Min. Mach.* **2020**, *48*, 66–70. [CrossRef]
22. Moncy, A.; Waldbjørn, J.P.; Berggreen, C. Biaxial Strain Control Fatigue Testing Strategies for Composite Materials. *Exp. Mech.* **2021**, *61*, 1193–1208. [CrossRef]
23. Zhao, H.; Feng, J.; Hang, T.; Liu, S.; Lin, J.; Li, H. Closed-loop Cross-compensation Control for Multi-channel Structural Fatigue Testing System. *Control Eng. China* **2021**, *28*, 2. [CrossRef]
24. Duan, J.; Shao, F.; Zhou, Y.; Zhang, Q. Controller of Fatigue Testing Machine for Aerospace Thermal Connections Based on Improved NSGA-III Algorithm. *Arab. J. Sci. Eng.* **2022**, *47*, 1873–1883. [CrossRef]
25. Napole, C.; Barambones, O.; Calvo, I.; Velasco, J. Feedforward Compensation Analysis of Piezoelectric Actuators Using Artificial Neural Networks with Conventional PID Controller and Single-Neuron PID Based on Hebb Learning Rules. *Energies* **2020**, *13*, 3929. [CrossRef]
26. Meng, F.; Hu, Y.; Ma, P.; Zhang, X.; Li, Z. Practical Control of a Cold Milling Machine Using an Adaptive PID Controller. *Appl. Sci.* **2020**, *10*, 2516. [CrossRef]
27. Qin, Y.; Duan, H. Single-Neuron Adaptive Hysteresis Compensation of Piezoelectric Actuator Based on Hebb Learning Rules. *Micromachines* **2020**, *11*, 84. [CrossRef]